



Introducing electromagnetic effects in Soledge3X

Raffael Düll, Hugo Bufferand, Eric Serre, Guido Ciraolo, Virginia Quadri,
Nicolas Rivals, Patrick Tamain

► To cite this version:

Raffael Düll, Hugo Bufferand, Eric Serre, Guido Ciraolo, Virginia Quadri, et al.. Introducing electromagnetic effects in Soledge3X. Contributions to Plasma Physics, 2024, pp.e202300147. 10.1002/ctpp.202300147 . hal-04474339

HAL Id: hal-04474339

<https://hal.science/hal-04474339>

Submitted on 23 Feb 2024

HAL is a multi-disciplinary open access archive for the deposit and dissemination of scientific research documents, whether they are published or not. The documents may come from teaching and research institutions in France or abroad, or from public or private research centers.

L'archive ouverte pluridisciplinaire **HAL**, est destinée au dépôt et à la diffusion de documents scientifiques de niveau recherche, publiés ou non, émanant des établissements d'enseignement et de recherche français ou étrangers, des laboratoires publics ou privés.



Distributed under a Creative Commons Attribution - NonCommercial - NoDerivatives| 4.0
International License

Introducing electromagnetic effects in Soledge3X

Raffael Düll¹ | Hugo Bufferand¹ | Eric Serre² | Guido Ciraolo¹ |
Virginia Quadri¹ | Nicolas Rivals¹ | Patrick Tamain¹

¹IRFM, CEA, Cadarache,
St-Paul-Lez-Durance, France

²CNRS, Centrale Marseille, M2P2,
Aix Marseille Université, Marseille, France

Correspondence

Raffael Düll, IRFM, CEA, Cadarache,
St-Paul-Lez-Durance, France.
Email: raffael.ellerdull@cea.fr

Funding information

EUROfusion, Grant/Award Number:
101052200; Aix Marseille Université,
Grant/Award Number:
ANR 10 EQPX 29 01

Abstract

In the pedestal region, electromagnetic effects affect the evolution of micro-instabilities and plasma turbulence. The transport code Soledge3X developed by the CEA offers an efficient framework for turbulent 3D simulation on an electrostatic model with a fixed magnetic field. The physical accuracy of the model is improved with electromagnetic induction, driven by the local value of the parallel component of the electromagnetic vector potential A_{\parallel} , known from Ampère's law. It is solved implicitly in a coupled system with the vorticity equation on the electric potential Φ . The consequence is a basic electromagnetic behavior in the form of shear Alfvén waves. A finite electron mass prevents unphysical speeds but requires solving for the time evolution of the parallel current density j_{\parallel} in the generalized Ohm's law. This term can be analytically included with little computational overhead in the system on Φ and A_{\parallel} and improves its numerical condition, facilitating the iterative solving procedure. Simulations on a periodic slab case let us observe the predicted bifurcation of the wave propagation speed between the Alfvén wave and the electron thermal wave speeds for varying perpendicular wavenumbers. The first results on a circular geometry with a limiter attest to the feasibility of turbulent electromagnetic scenarios.

KEYWORDS

electromagnetism, Soledge3X, turbulent simulations

1 | INTRODUCTION

Studying the heat exhaust of large magnetic fusion devices requires a good understanding of turbulence in the tokamak edge region. Experimental studies have demonstrated that plasma filaments are responsible for the transport of hot plasma particles over large distances beyond the separatrix.^[1,2] Electromagnetic effects play a key role in driving plasma turbulence in the pedestal region, especially when approaching the L-H transition. They affect the filamentary structure of turbulent plasma blobs in the scrape-off layer.^[3–5] Characteristics of drift Alfvén turbulence and its effect in tokamak edge plasma were extensively described by Scott in the past years.^[6–8]

It is, therefore, no surprise that many code projects with the fluid-drift approach such as BOUT++,^[9] GRILLIX,^[10] or GBS^[11] approach use an electromagnetic model to some extent. Electromagnetic effects can typically manifest under two forms: magnetic induction, which provokes shear Alfvén waves, and electromagnetic flutter, which perturbs magnetic field lines. This work will focus on the implementation of the inductive model in Soledge3X.

This is an open access article under the terms of the [Creative Commons Attribution-NonCommercial-NoDerivs](https://creativecommons.org/licenses/by-nc-nd/4.0/) License, which permits use and distribution in any medium, provided the original work is properly cited, the use is non-commercial and no modifications or adaptations are made.

© 2024 The Authors. *Contributions to Plasma Physics* published by Wiley-VCH GmbH.

2 | THE ELECTROMAGNETIC MODEL IN SOLEDGE3X

Soledge3X is a multispecies 3D transport code that allows to study various aspects of edge plasma such as turbulent transport,^[12,13] plasma-neutral interaction,^[14] or impurity transport.^[15] The magnetic configuration is assumed to be toroidally symmetrical and is fixed in time. Under these circumstances, the unit magnetic field vector $\mathbf{b} = \mathbf{B}/B$ has always a zero value in its radial component. Spatial operators are commonly applied in either parallel or perpendicular directions; therefore, introducing the operators $\nabla_{\parallel} = \mathbf{b} \cdot \nabla$ and $\nabla_{\perp} = \nabla - \mathbf{b} \nabla_{\parallel}$ contributes to the readability of the upcoming equations.

2.1 | Conservative equations

The Soledge3X model discretizes Braginskii equations^[16] to a finite volume method in which flux balances are calculated at each cell face before solving the conservative equation in the corresponding cells. These equations are provided for the ion density n_i , the ion momentum in parallel direction $m_i v_{\parallel,i}$ and both the ion and electron energies ε_{α} :

$$\partial_t n_i + \nabla \cdot [n_i (v_{\parallel,i} \mathbf{b} + \mathbf{v}_{\perp,i})] = S_{n_i} \quad (1)$$

$$\partial_t [m_i n_i v_{\parallel,i}] + \nabla \cdot [m_i n_i v_{\parallel,i} (v_{\parallel,i} \mathbf{b} + \mathbf{v}_{\perp,i})] = -\nabla_{\parallel} p_i + Z_i e n_i E_{\parallel} - \mathbf{b} \cdot \nabla \cdot \bar{\bar{\Pi}}_i + R_{\parallel} + S_{\Gamma_{\parallel,i}} \quad (2)$$

$$\partial_t \varepsilon_{\alpha} + \nabla \cdot \left[(\varepsilon_{\alpha} + p_{\alpha}) (v_{\parallel,\alpha} \mathbf{b} + \mathbf{v}_{\perp,\alpha}) + \bar{\bar{\Pi}}_{\alpha} \cdot (v_{\parallel,\alpha} \mathbf{b} + \mathbf{v}_{\perp,\alpha}) + \mathbf{q}_{\alpha} \right] = (v_{\parallel,\alpha} \mathbf{b} + \mathbf{v}_{\perp,\alpha}) \cdot (n_{\alpha} \mathbf{E}_{\alpha} + \mathbf{R}) + Q + S_{\varepsilon_{\alpha}} \quad (3)$$

In this set of equations, the density and momentum source terms S_{n_i} and S_{Γ_i} originate from ionization and recombination processes, the stress tensor $\bar{\bar{\Pi}}_i$ comprises parallel ion viscous effects, perpendicular anomalous viscosity, and diamagnetic effects and R_{\parallel} is a friction force from the Zhdanov closure. The total energy corresponds to the sum of thermal and parallel kinetic energy $\varepsilon_{\alpha} = \frac{3}{2} e n_{\alpha} T_{\alpha} + \frac{1}{2} m_{\alpha} n_{\alpha} v_{\parallel,\alpha}^2$ and the heat flux \mathbf{q}_{α} has collisional and a diamagnetic components. The electron density is not explicitly solved but can be retrieved from the charge-weighted sum of ion densities under the quasi-neutrality assumption. A similar operation is performed for the electron momentum if we assume an ambipolar plasma.

In the conservative (Equations 1–3), the velocity vector is split into its parallel and perpendicular components. This is because $v_{\parallel,i}$ is obtained by solving the momentum conservation equation, but the perpendicular part $\mathbf{v}_{\perp,i} = \mathbf{b} \times (\mathbf{v}_i \times \mathbf{b})$ requires the drift-ordering assumption. With the values of the pressure p_i and the electric potential Φ from the previous timestep, the first-order drift is the sum of the “E cross B” and diamagnetic drift velocities:

$$\mathbf{v}_{\perp,i}^{(0)} = \mathbf{v}_E + \mathbf{v}_i^* = \frac{\mathbf{E} \times \mathbf{B}}{B^2} + \frac{\mathbf{B} \times \nabla p_i}{e n Z B^2} \quad (4)$$

A second-order drift can then be calculated by summing the polarization, the friction force, and the parallel viscous stress drifts which all require $\mathbf{v}_{\perp,i}^{(0)}$.

2.2 | Charge balance equation

In the electrostatic approach, the “E cross B” drift in Equation (4) requires the perpendicular gradient of the electric potential $\mathbf{E}_{\perp} = -\nabla_{\perp} \Phi$. It can be derived from the quasi-neutral charge balance equation where the divergence of the total current vanishes $\nabla \cdot \mathbf{j}^{tot} = 0$. The current density is defined as $\mathbf{j}^{tot} = \sum_{\alpha} q_{\alpha} n_{\alpha} \mathbf{v}_{\alpha}$, and as for the velocity, it is decomposed in parallel and perpendicular components. We then have the following equation where friction and viscous stress currents are omitted:

$$\nabla \cdot [j_{\parallel} \mathbf{b} + \mathbf{j}_{\perp}^* + \mathbf{j}_{\perp,pola}] = 0 \quad (5)$$

For the polarization current, we need to introduce the vorticity Ω of the first-order drift velocity, dependent on the cyclotronic frequency ω_c .

$$\Omega = \nabla \cdot \sum_i \left[-q_i \left(\frac{\mathbf{b}}{\omega_c} \right) \times \left(n_i \mathbf{v}_i^{(0)} \right) \right] \quad (6)$$

The divergence of $\mathbf{j}_{\perp, \text{pola}}$ is then the total time derivative of the vorticity,^[17] which can be decomposed in $\nabla \cdot \mathbf{j}_{\perp, \text{pola}} = -\partial_t \Omega + \nabla \cdot \mathbf{j}_{\Omega}$. The current \mathbf{j}_{Ω} corresponds to the vorticity flux. We finally have

$$\nabla \cdot \mathbf{j}_{\perp, \text{pola}} = -\partial_t \nabla \cdot \sum_i \left[\frac{m_i n_i}{q_i B^2} \nabla_{\perp} \Phi + \frac{m_i}{q_i B^2} \nabla_{\perp} p_i \right] + \nabla \cdot \mathbf{j}_{\Omega} \quad (7)$$

The diamagnetic current \mathbf{j}_{\perp}^* is obtained from the diamagnetic drift velocity \mathbf{v}_i^* in Equation (4). The equation on the parallel current is derived from the difference of the parallel momentum balances (Equation 2) for electrons and ions. It carries the main modification with the introduction of the electromagnetic model which will be detailed in the next sections.

2.2.1 | Electrostatic vorticity equation

In the current electrostatic model, the parallel current is given by Ohm's law with neglected electron mass:

$$j_{\parallel} = \sigma_{\parallel} \left(E_{\parallel} + \frac{1}{en_e} \nabla p_e - \frac{1}{en_e} R_e \right) \quad (8)$$

The parallel electric field is calculated as $E_{\parallel} = -\nabla_{\parallel} \Phi$, and the parallel conductivity σ_{\parallel} and the thermal force $R_e = -0.71 n_e \nabla_{\parallel} T_e$ are obtained from Branginskii's closure. If we plug this into the charge balance (Equation 5), we obtain a system on the electric potential Φ :

$$\partial_t \nabla \cdot \sum_i \left[\frac{m_i n_i}{B^2} \nabla_{\perp} \Phi \right] + \nabla \cdot [\sigma_{\parallel} \nabla_{\parallel} \Phi] \mathbf{b} = \nabla \cdot \left[\frac{T_e}{e} \nabla_{\parallel} \log n_e + \frac{1.71}{e} \nabla_{\parallel} T_e \right] \mathbf{b} + \text{RHS} \quad (9)$$

The generic right-hand side term contains all remaining terms from the vorticity evolution 7 and the charge balance 5 that are not essential in this discussion. The system is solved implicitly for the potential Φ at each timestep and it becomes apparent that both a parallel and perpendicular Laplacian need to be solved on the potential Φ . The ratio of the diffusion coefficients $\sigma_{\parallel} B^2 / (m_i n_i \partial_t)$ typically reaches very large values above 10^6 leading to an anisotropic system that challenges the converge behavior of iterative solvers.

2.2.2 | Electromagnetic vorticity equation

The electrostatic model is extended by electromagnetic induction effects. For this purpose, we need to introduce the parallel magnetic vector potential A_{\parallel} to the system whose curl corresponds to the magnetic field:

$$\nabla \times \mathbf{A} = \mathbf{B} \quad (10)$$

Because parallel scales are much larger than perpendicular ones, we only consider the parallel projection $A_{\parallel} = \mathbf{A} \cdot \mathbf{b}$. In the Coulomb gauge, the electromagnetic potential, Ampère's law links A_{\parallel} to the current density $\nabla \cdot \nabla_{\perp} A_{\parallel} = -\mu_0 j_{\parallel}$ and the rate of change of A_{\parallel} enters the definition of the parallel electric field $E_{\parallel} = -\nabla_{\parallel} \Phi - \partial_t A_{\parallel}$. The former completes the vorticity system with a new equation on A_{\parallel} while the latter affects the expression of the electric field in Ohm's law (8).

In addition, Dudson et al.^[18] suggested a finite electron mass to stabilize Alfvénic dynamics, that results in an electron inertia term in Ohm's law. The new set of equations with electromagnetic induction and electron inertia then reads

$$\nabla \cdot \left[\frac{m_i n_i}{B^2} \partial_t \nabla_{\perp} \Phi \right] = \nabla \cdot (j_{\parallel} \mathbf{b}) + RHS \quad (11)$$

$$j_{\parallel} + \frac{\sigma_{\parallel} m_e}{n_e e^2} \left(\frac{\partial j_{\parallel}}{\partial t} - \nabla \cdot (\nu_e \nabla_{\perp} j_{\parallel}) \right) = \sigma_{\parallel} \left(-\nabla_{\parallel} \Phi - \partial_t A_{\parallel} + \frac{T_e}{e} \nabla_{\parallel} \log(n_e) + \frac{1.71}{e} \nabla_{\parallel} T_e \right) \quad (12)$$

$$\Delta_{\perp} A_{\parallel} = -\mu_0 j_{\parallel} \quad (13)$$

The perpendicular diffusion on j_{\parallel} with coefficient ν_e emanates from the anomalous viscous transport in the ion momentum (Equation 2) and a specific diffusion coefficient can be defined for electrons that may improve the numerical stability.

3 | IMPLEMENTATION OF THE MODEL

In the original Soledge3X model, the parallel current density j_{\parallel} did not exist as a proper variable because its expression was hidden in various terms of the vorticity equation. The electromagnetic potential A_{\parallel} in turn is entirely new to the model. Both scalar fields need to be added to the model and their implementation raises some peculiarities about the meshing and the coupled implicit 3D vorticity system that will be discussed here.

3.1 | Numerical treatment of the electromagnetic vorticity equation

The new fields A_{\parallel} and j_{\parallel} must be nondimensionalized according to the existing model. We choose the electromagnetic potential to be homogeneous to the current density from Ampere's law 13. We further introduce the reference ratio β_0 to conveniently use \hat{A}_{\parallel} in Ohm's law. Together with the reference density n_0 , the reference thermal speed $c_0 = \sqrt{eT_0/m_u}$ the Larmor radius ρ_0 and the reference magnetic field strength B_0 , we get

$$j_{\parallel,0} = en_0 c_0 \quad A_{\parallel,0} = \mu_0 en_0 c_0 \rho_0^2 \quad \beta_0 = \frac{en_0 T_0}{B_0^2 / \mu_0} \quad (14)$$

The dimensionless fields $\hat{\Phi}$, \hat{A}_{\parallel} , and \hat{j}_{\parallel} are then solved implicitly in time. A coupled system on the two potentials needs to be solved on the full 3D domain to compute their new values:

$$\begin{pmatrix} \hat{\nabla} \cdot [\hat{D}_{\perp} \hat{\nabla}_{\perp} \circ] + \hat{\nabla} \cdot [\hat{D}_{\parallel} \hat{\nabla}_{\parallel} \circ \mathbf{b}] & \frac{\beta_0}{\hat{\delta}_t} \hat{\nabla} \cdot [\hat{D}_{\parallel} \circ \mathbf{b}] \\ \hat{D}_{\parallel} \circ & \frac{\beta_0}{\hat{\delta}_t} \hat{D}_{\parallel} \circ - \hat{\nabla} \cdot [\hat{\nabla}_{\perp} \circ] \end{pmatrix} \begin{pmatrix} \hat{\Phi}^{new} \\ \hat{A}_{\parallel}^{new} \end{pmatrix} = \begin{pmatrix} \hat{\nabla} \cdot [\hat{D}_{\parallel}^{old} \mathbf{b}] + \hat{\nabla} \cdot [\hat{D}_{\perp} \hat{\nabla}_{\perp} \hat{\Phi}^{old}] + \frac{\beta_0}{\hat{\delta}_t} \hat{\nabla} \cdot [\hat{D}_{\parallel} \hat{A}_{\parallel}^{old} \mathbf{b}] + RHS^{\Phi} \\ \hat{D}_{\parallel}^{old} + \frac{\beta_0}{\hat{\delta}_t} \hat{D}_{\parallel} \hat{A}_{\parallel}^{old} + RHS^{A_{\parallel}} \end{pmatrix} \quad (15)$$

with : $\hat{D}_{\perp} = \frac{m_i n_i}{B^2 \hat{\delta}_t}$, $\hat{D}_{\parallel} = \frac{\hat{\sigma}_{\parallel} \hat{n}_e \hat{\delta}_t}{\hat{n}_e \hat{\delta}_t + \hat{\sigma}_{\parallel} \hat{m}_e}$ and $\hat{D}_t = \frac{\hat{\sigma}_{\parallel} \hat{m}_e}{\hat{n}_e \hat{\delta}_t + \hat{\sigma}_{\parallel} \hat{m}_e}$

The parameter $\hat{\delta}_t$ depends on the time-stepping scheme and equals the timestep size only for a first-order implicit Euler method. Analogously, the terms labeled with \circ^{old} correspond to a combination of the values at the previous timesteps, or simply the last calculated value for the implicit Euler method. Once the system has been solved for Φ and A_{\parallel} , the new value for the parallel current $\hat{j}_{\parallel}^{new}$ is retrieved employing Ohm's law (12); hence, the scheme is equally implicit for \hat{j}_{\parallel} .

The top left block matrix in Equation (15) along with the upper right-hand-side vector corresponds to the electrostatic vorticity system 9. The major difference appears within the parallel diffusion coefficient D_{\parallel} where electron inertial terms complement the parallel conductivity σ_{\parallel} . By construction, D_{\parallel} is always smaller than σ_{\parallel} and the difference is more pronounced for low timestep sizes. This reduces the anisotropy, improves the condition of the system, and should facilitate the convergence of iterative solvers.

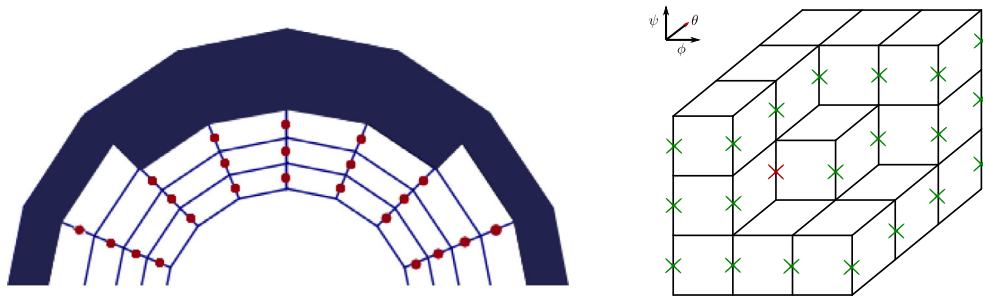


FIGURE 1 Schemes of the staggered mesh. Conventional fields (e.g., n , T , and Φ) are defined at the centres of the depicted cells. The left scheme shows a general limiter configuration on a poloidal plane with cells in the tokamak wall filled. Staggered points are not defined on the sheath domain boundary. The right scheme is a three-dimensional view of the meshing. The red cross shows the position of the staggered point corresponding to the central cell in the depicted $3 \times 3 \times 3$ block.

3.2 | Discretization and boundary conditions

One specificity in Soledge3X is the field-aligned coordinate system in which a structured grid is aligned with magnetic flux surfaces. Each point in the domain is hence uniquely defined by a set of one radial, one poloidal, and one toroidal index $[i_\psi, i_\theta, i_\phi]$. In Equations (11)–(13), A_\parallel and j_\parallel appear to be one spatial derivative in parallel direction away from the remaining fields. To take advantage of compact finite differences in the finite volume method they are defined in poloidally and toroidally staggered cells. Figure 1 illustrates the construction of this staggered grid from the regular centered meshing.

Staggered mesh points overlap with the domain boundary at the sheath where equilibrium magnetic field lines intersect the wall. These points are however not solved in the implicit system from Subsection 3.1, as their values for A_\parallel^{BC} and j_\parallel^{BC} are calculated otherwise. The electromagnetic potential drives perturbations that we assume to vanish in direct vicinity to the wall; hence, we enforce Dirichlet boundary conditions $A_\parallel^{BC} = 0$. For coherence with the finite electron mass in Ohm's law, we need to consider inertial effects on the sheath current $\left(1 + \frac{m_e}{n_e e^2} \partial_t\right) j_\parallel^{BC} = j_{sat} (1 - e^{\Lambda - \Phi/T_e})$. This current is calculated in the vorticity equation by linearizing $\hat{\Phi}$.

4 | MODEL VERIFICATION

The new electromagnetic model was first verified with an analytic solution and then validated with a linear test case.

4.1 | Method of manufactured solutions

The method of manufactured solutions (MMS)^[19] offers a convenient framework to compare a numerical model with its exact solution. It stipulates adding analytic source terms to the right-hand side of a PDE to compensate for all numerical operators that appear in the model. In our case, we define a three-dimensional distorted mesh on a toroidal magnetic configuration with arbitrary initial profiles for all plasma fields. The source terms described in the MMS approach are added to all time-independent terms of the model (11)–(13) to conserve a steady state. If we now compare the initial plasma distribution with any subsequent timestep, we can evaluate the error induced by the numerical scheme. Moreover, if we adjust the resolution of the discretization, the change in the calculated error indicates the order of convergence of the numerical scheme, which shall be close to the theoretical value of two.

Between each scenario, the number of cells per direction is increased by a factor ~ 1.3 , using periodic boundary conditions in poloidal and toroidal direction and Dirichlet boundary conditions radially to prescribe the analytic solution there. Fields are initialized with a sinusoidal distribution centered around a realistic reference value and we let the simulation run for one single timestep. The relative truncation error is then calculated for the fields of interest A_\parallel , j_\parallel , and Φ .

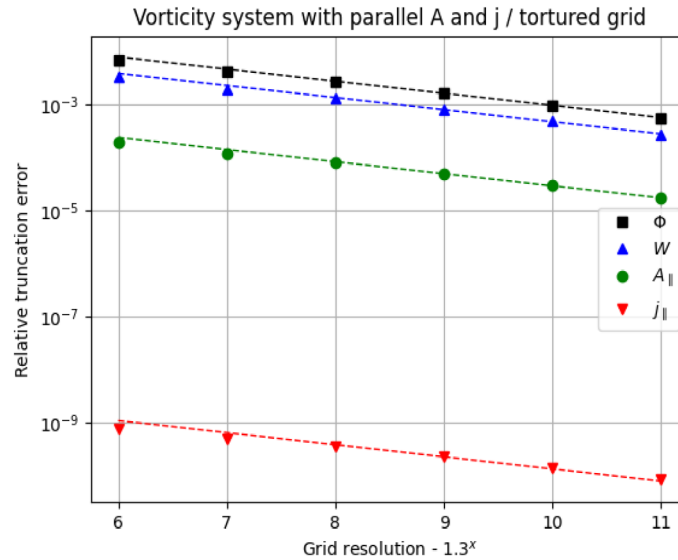


FIGURE 2 Error and convergence of the MMS model. The points show the estimated error while the dashed line indicates the slope of the theoretic second-order convergence.

as well as the connected vorticity Ω . We observe an excellent agreement in Figure 2 between the calculated error and its predicted quadratic decrease, showing that the new staggered operators have been properly implemented.

4.2 | Linear analysis

A more comprehensive test would be to show that the model can reproduce basic linear plasma behavior. To this effect, we consider a standard four-field model that couples the electron density n_e with the parallel current density $j_{||}$ and both potentials Φ and $A_{||}$. The governing equations now are

$$\begin{aligned} \nabla \cdot \left[\frac{m_i n_i}{B^2} \partial_t \nabla_{\perp} \Phi \right] &= \nabla \cdot (j_{||} \mathbf{b}) & \Delta_{\perp} A_{||} &= -\mu_0 j_{||} \\ j_{||} + \frac{\sigma_{||} m_e}{n_e e^2} \partial_t j_{||} &= \sigma_{||} \left(-\nabla_{||} \Phi - \partial_t A_{||} + \frac{T_e}{e} \nabla_{||} \log(n_e) \right) & \partial_t n_e &= \frac{1}{e} \nabla \cdot j_{||} \end{aligned} \quad (16)$$

It is essentially an isothermal variant of the original system in Equations (11)–(13) without curvature effects. Its complex dispersion relation has a real and an imaginary part indicating the appearance of a decaying wave. The wave frequency depends on the parallel and perpendicular wave numbers $k_{||}$ and k_{\perp} , linked to the respective Laplacian terms.

$$\omega_0^2 = \frac{\frac{B^2}{m_i} + \frac{T_0}{e} k_{\perp}^2}{n_e \mu_0 + \frac{m_e}{e^2} k_{\perp}^2} k_{||}^2 - \frac{k_{\perp}^4}{4\sigma_{||}^2 \left(\mu_0 + \frac{m_e}{e^2 n_i} k_{\perp}^2 \right)^2} \quad (17)$$

In cases with high parallel conductivity, the first term dominates the dispersion relation. We then observe that the relation describes a wave in parallel direction whose velocity is bound by the Alfvén wave speed $v_A = \frac{B}{\sqrt{m_i n_i \mu_0}}$ for small k_{\perp} and by the thermal electron wave speed $v_{th,e} = \sqrt{\frac{e T_e}{m_e}}$ for large k_{\perp} . This is in line with the findings by Dudson et al.^[18] and reflects the need for electron inertia to avoid unphysically large speeds in the upper k_{\perp} limit.

To best observe the dispersion relation in an actual simulation, we set up a 3D slab domain with periodic boundary conditions in all three spatial directions. A uniform magnetic field acts in a diagonal direction in the $\theta - \varphi$ plane, hence no curvature effects act on the plasma. The electron density is initialized with the 3D wave profile for the mode (1). The same profile appears quickly after on the three remaining fields from the model 16 and a decaying standing wave evolves

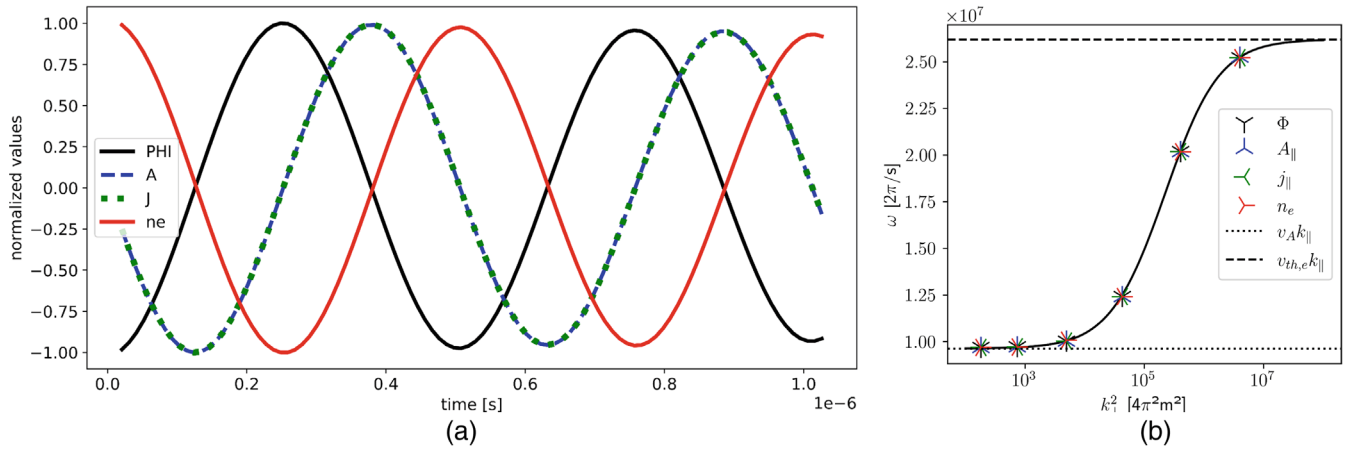


FIGURE 3 Behavior of the 3D SLAB model with 63 cells per direction and periodic boundary conditions everywhere. We apply an initial wave profile for the density and let the system 16 evolve accordingly. (a) Evolution of the normalized perturbation amplitude for every field. (b) Fitted wave frequencies for different perpendicular wave numbers at a fixed parallel wave number. The solid lines indicates the expected frequency from the dispersion relation (17).

as it appears in Figure 3a. With the electron density as a reference, the electric potential Φ evolves with the opposite phase, while the electromagnetic vector potential A_{\parallel} and the parallel current density j_{\parallel} have the same $\pi/2$ phase shift.

By construction, the slab dimensions define the cartesian wavenumbers k_{ψ} , k_{θ} , and k_{φ} . Together with the uniform magnetic field, we can express the squares of the directional wavenumbers in the dispersion relation 17:

$$k_{\parallel} = b_{\theta} k_{\theta} + b_{\varphi} k_{\varphi} \quad k_{\perp}^2 = (k_{\psi} + k_{\theta} + k_{\varphi})^2 - k_{\parallel}^2 \quad (18)$$

To reproduce the transition from Alfvén to thermal electron waves as in Stegmeir et al.,^[10] we fix k_{\parallel} and modify the radial slab dimension to compare the wave behavior at different perpendicular wavenumbers k_{\perp} . After a sufficient number of iterations, the wave frequency is fitted with a least squares method to the profile. The transition between Alfvén and thermal electron waves is visible in Figure 3b, and the fitted frequencies for all four fields match well with the predicted value along the solid line.

5 | FIRST SIMULATIONS ON A LIMITER SCENARIO

Now that the correct implementation has been verified, we will have a glimpse at how the electromagnetic model behaves in a more realistic geometry. We consider a torus with an outer radius of 0.6 m, where we simulate edge plasma comprised between the inner radii 0.12 and 0.24 m. There is an outer limiter that extends into the plasma up to an inner radius of 0.2 m and the toroidal magnetic field has a strength of 1 T. The plasma is composed of electrons and deuterium ions with a constant density and energy source inside the separatrix to excite turbulence. Radial transport is carried by “ExB” and “gradB” drifts. The mesh has 128 cells in radial, 512 in poloidal, and 32 in toroidal direction, where we only consider a 1/4 of a torus.

5.1 | Electromagnetic snapshots

To achieve an electromagnetic simulation, an electrostatic turbulent scenario is restarted after a few 100 timesteps. Steady-state Ohm’s 12 and Ampère’s 13 laws give a reasonable guess for the initial distributions of respectively j_{\parallel} and A_{\parallel} at the restart. The plasma β depends on the local plasma conditions and reaches values of about 0.1%, and electron inertia effects rely on a physically accurate mass ratio $m_e/m_u \approx 5.5 \cdot 10^{-4}$. Typical simulation snapshots for the described circular scenario are shown in Figure 4. Turbulent structures appear and take a filamentary structure that expands radially.

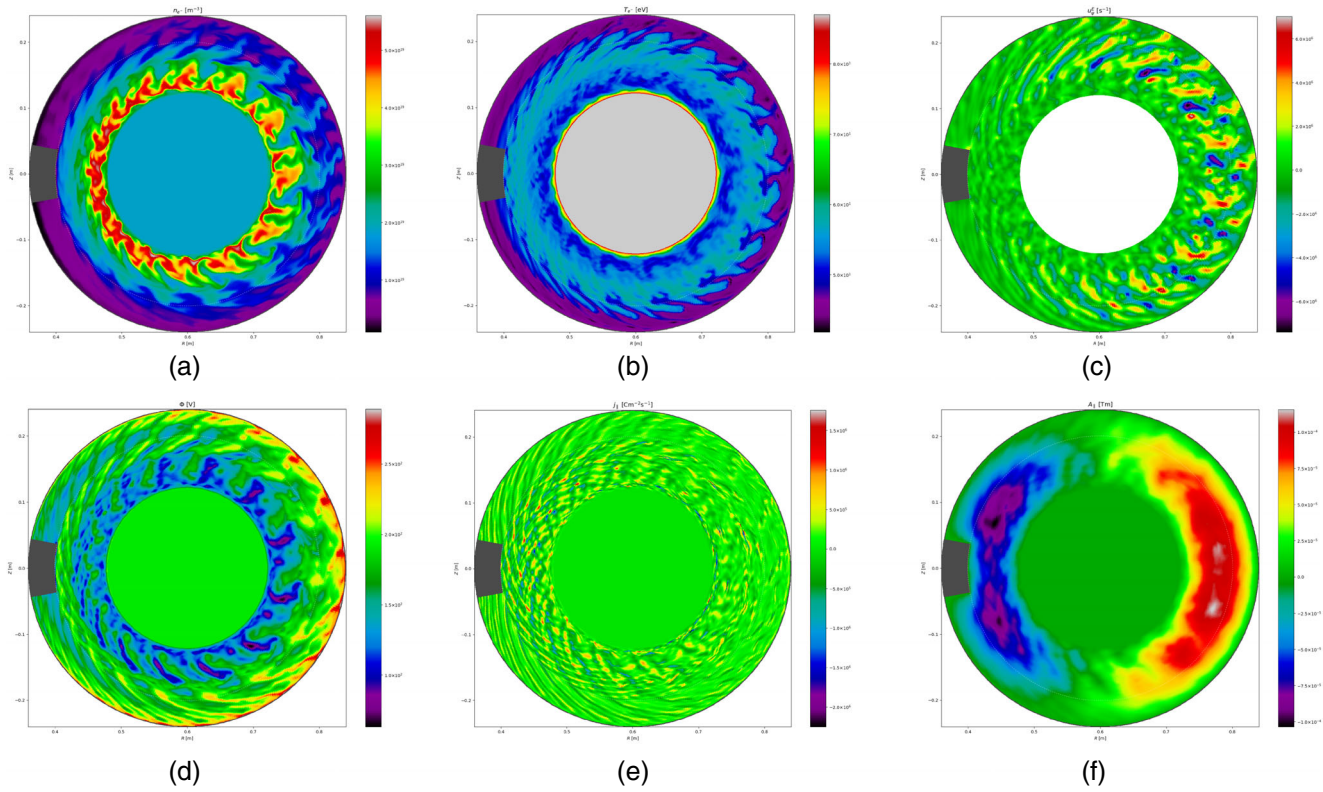


FIGURE 4 Snapshots of poloidal planes with established electromagnetic turbulent profiles on a toroidal geometry with an outer limiter. Results are shown after 0.8 ms simulated time. (a) electron density n_e . (b) electron temperature T_e . (c) Radial ExB drift u_{ψ}^{EB} . (d) Electric potential Φ . (e) Parallel current density $j_{||}$. (f) Parallel electromagnetic potential $A_{||}$.

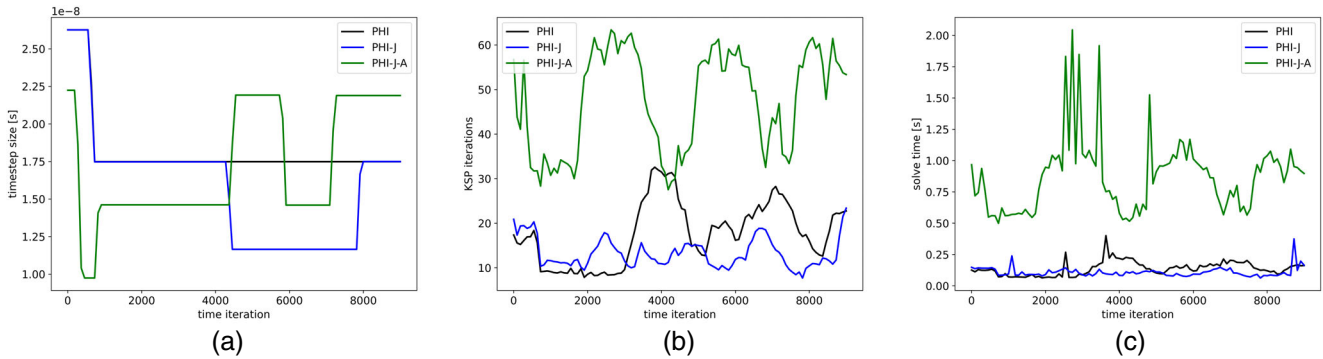


FIGURE 5 Evolution of the following numerical parameters over time iterations on the turbulent limiter scenario: (a) Time step size. (b) Number of iterations of the implicit solver on the 3D limiter scenario. (c) Solve time of the implicit solver.

5.2 | Numerical observations

Electron inertia and electromagnetic induction can be switched on and off independently in the model 11–13. This section aims to compare the numerical behavior of the code in each scenario. One key aspect of the implicit treatment in Soledge3X is the coupled system 15 between Φ and $A_{||}$. Compared with the electrostatic case, the 3D operator doubles the number of unknowns to accommodate both potentials which will inevitably impact the code performance. The simulation is run on The biconjugate gradient stabilized method^[20] (KSP-BCGS) with the geometric algebraic multi-grid (PC-GAMG) preconditioner from the PETSc^[21] iteratively solving the extended vorticity problem. The simulation is executed on 384 computing cores on 8 nodes of the MARCONI computing centre.^[22]

We run a pure electrostatic simulation (PHI), an electrostatic with electron inertia (PHI-J) and an electromagnetic with electron inertia (PHI-J-A). The simple electromagnetic scenario with zero electron mass is missing because of critical numerical instabilities, which is the first hint at the benefits of electron inertia. Figure 5 shows the evolution of the timestep size, the number of KSP iterations until convergence and the PETSc solve time for the vorticity system. The timestep size, driven by the CFL condition derived from particle, momentum, and energy fluxes, takes similar values for all three cases, indicating that the fluxes are not severely impacted by magnetic induction or electron inertia. On the other hand, the number of iterations the iterative solver needs to converge depends on the chosen scenario. The PHI and PHI-J cases roughly follow the same pattern with occasional peaks. On average, the case with electron inertia requires slightly fewer iterations thanks to the reduction in anisotropy of the vorticity equation (explanations in Subsection 3.1). The electromagnetic case however needs twice as many iterations to converge on average, which can be explained by the more complex matrix structure that covers two coupled systems in the inherent challenges it poses for the iterative solver. These observations are reflected in the solve time of the vorticity system which is significantly higher in the electromagnetic scenario. Not only does the solver need more iterations, but the system has doubled in size which negatively impacts the solve time. Despite of the performance degradations, this implicit procedure for electromagnetic simulations is appropriate as the additional costs remain reasonable.

6 | CONCLUSION

A new electromagnetic model was implemented in the Soledge3X code, introducing magnetic induction and electron inertia. For this purpose, two new fields are now solved implicitly with the electric potential Φ in the vorticity equation: the parallel electromagnetic vector potential A_{\parallel} and the parallel current density j_{\parallel} . They are defined on a poloidally and staggered grid and require a new set of adapted numerical operators whose correct second-order implementation could be verified with the MMS approach. The new model introduces basic electromagnetic plasma behavior in the form of shear Alfvén waves that could be accurately measured in a linear model on a three-dimensional cartesian slab domain. Successful simulations on a circular limiter scenario show that the electromagnetic model can be used along with “ExB”-drifts for turbulence analysis.

The implicit approach avoids new limitations on the CFL condition and allows us to keep the flux-driven timestep size. Considering a finite electron mass has proven to be essential for numerical stability. By design of the coupled implicit system, it reduces the anisotropy of the vorticity problem, and we could already observe an improved convergence behavior of the iterative solver in the electrostatic scenario with electron inertia. In the full electromagnetic setting, however, the coupling between the vorticity equation and Ampère’s law adds complexity to the solving procedure and consequently increases the effective solve time. The performance degradation remains acceptable and is worth the additional physics.

In future work, the staggered operators need to be extended to the X-point geometry to achieve electromagnetic simulations on realistic domains for diverted tokamaks. An in-depth analysis of the impact of magnetic induction on turbulent growth rates may replicate observations on faster-growing perturbations of the electric potential.^[23] The now-available electromagnetic potential A_{\parallel} allows us to calculate perturbations of the equilibrium magnetic field, introducing flutter phenomena to the model. This could help to stabilize turbulent profiles even in low- β plasmas^[24] and opens the path to study resonant magnetic perturbations (RMP)^[25] or radial heat transport at the targets.^[26]

ACKNOWLEDGEMENTS

This work has been carried out within the framework of the EUROfusion Consortium, funded by the EUROfusion (Grant Agreement No 101052200). Views and opinions expressed are however those of the authors only and do not necessarily reflect those of the European Union or the European Commission. Neither the European Union nor the European Commission can be held responsible for them. This work was granted access to the HPC resources of the EUROfusion High Performance Computer (Marconi-Fusion) under the project TSVV3. This work was granted access to the HPC/AI resources of CINES/IDRIS/TGCC under the allocation 2022 A0120510482 made by GENCI and to the HPC resources of Aix Marseille Université financed by the project Equip@Meso (ANR 10 EQPX 29 01).

CONFLICT OF INTEREST STATEMENT

The authors declare no potential conflicts of interests.

DATA AVAILABILITY STATEMENT

The data that support the findings of this study are available from the corresponding author upon reasonable request.

REFERENCES

- [1] B. D.udson, N. Ben Ayed, A. Kirk, H. R. Wilson, G. Counsell, X. Xu, M. Umansky, P. B. Snyder, B. Lloyd, the MAST team, *Plasma Phys. Control. Fusion* **2008**, 50, 124012.
- [2] I. Furno, B. Labit, M. Podestà, A. Fasoli, S. H. Müller, F. M. Poli, P. Ricci, C. Theiler, S. Brunner, A. Diallo, J. Graves, *Phys. Rev. Lett.* **2008**, 100, 055004.
- [3] W. Lee, J. Angus, M. V. Umansky, S. I. Krashenninnikov, *J. Nucl. Mater.* **2015**, 463, 765.
- [4] F. Militello, B.udson, L. Easy, A. Kirk, P. Naylor, *Plasma Phys. Control. Fusion* **2017**, 59, 125013.
- [5] A. Ross, A. Stegmeir, P. Manz, D. Grosej, W. Zholobenko, D. Coster, F. Jenko, *Phys. Plasmas* **2019**, 26, 102308.
- [6] B. D. Scott, *Plasma Phys. Control. Fusion* **1997**, 39, 1635.
- [7] B. D. Scott, *Plasma Phys. Control. Fusion* **2003**, 45, A385.
- [8] B. D. Scott, *Plasma Phys. Control. Fusion* **2007**, 49, S25.
- [9] B. D.udson, A. Allen, G. Breyiannis, E. Brugger, J. Buchanan, L. Easy, S. Farley, I. Joseph, M. Kim, A. D. McGann, J. T. Omotani, M. V. Umansky, N. R. Walkden, T. Xia, X. Q. Xu, *J. Plasma Phys.* **2015**, 81, 365810104.
- [10] A. Stegmeir, A. Ross, T. Body, M. Francisquez, W. Zholobenko, D. Coster, O. Maj, P. Manz, F. Jenko, B. N. Rogers, K. S. Kang, *Phys. Plasmas* **2019**, 26, 052517.
- [11] M. Giacomini, P. Ricci, A. Corrado, G. Fourestey, D. Galassi, E. Lanti, D. Mancini, N. Richart, L. N. Stenger, N. Varini, *J. Comput. Phys.* **2022**, 463, 111294.
- [12] P. Tamain, H. Bufferand, G. Ciraolo, C. Colin, D. Galassi, P. Ghendrih, F. Schwander, E. Serre, *J. Comput. Phys.* **2016**, 321, 606.
- [13] H. Bufferand, J. Bucalossi, G. Ciraolo, G. Falchetto, A. Gallo, P. Ghendrih, N. Rivals, P. Tamain, H. Yang, G. Giorgiani, F. Schwander, M. Scotto d'Abusco, E. Serre, Y. Marandet, M. Raghunathan, *Nucl. Fusion* **2021**, 61, 116052.
- [14] N. Rivals, P. Tamain, Y. Marandet, X. Bonnin, H. Bufferand, R. A. Pitts, G. Falchetto, H. Yang, G. Ciraolo, *Contrib. Plasma Physics* **2022**, 262, 101293.
- [15] G. Ciraolo, S. di Genova, H. Yang, A. Gallo, N. Fedorczak, H. Bufferand, J. P. Gunn, P. Tamain, R. Guirlet, C. Guillemaut, C. Desgranges, C. Bourdelle, E. Tsitrone, J. Bucalossi, M. Scotto D'Abusco, E. Serre, Y. Marandet, M. Raghunathan, A. Sepetys, J. Romazanov, A. Kirschner, S. Brezinsek, *Nucl. Fusion* **2021**, 61, 126015.
- [16] S. I. Braginskii, *Rev. Plasma Phys.* **1965**, 1, 205.
- [17] H. Bufferand, C. Baudoin, J. Bucalossi, G. Ciraolo, J. Denis, N. Fedorczak, D. Galassi, P. Ghendrih, R. Leybros, Y. Marandet, N. Mellet, J. Morales, N. Nace, E. Serre, P. Tamain, M. Valentinuzzi, *Nucl. Mater. Energy* **2017**, 12, 852–. Proceedings of the 22nd International Conference on Plasma Surface Interactions 2016, 22nd PSI.
- [18] B. D.udson, S. L. Newton, J. T. Omotani, J. Birch, *Plasma Phys. Control. Fusion* **2021**, 63, 125008.
- [19] P. J. Roache, in *Computer Simulation Validation: Fundamental Concepts, Methodological Frameworks, and Philosophical Perspectives* (Eds: C. Beisbart, N. J. Saam), Springer Nature Switzerland AG, Cham, **2019**, p. 295.
- [20] H. A. van der Vorst, *SIAM J. Sci. Stat. Comput.* **1992**, 13, 631.
- [21] S. Balay, S. Abhyankar, M. F. Adams, et al., PETSc Web page. **2023** <https://petsc.org/>
- [22] F. Iannone, G. Bracco, C. Cavazzoni, R. Coelho, D. Coster, O. Hoenen, A. Maslennikov, S. Migliori, M. Owsiak, A. Quintiliani, B. Palak, V. Pais, F. Robin, E. Rossi, I. Voitsekhovitch, *Fusion Eng. Des.* **2018**, 129, 354.
- [23] R. Hager, S. Ku, A. Y. Sharma, C. S. Chang, R. M. Churchill, A. Scheinberg, *Phys. Plasmas* **2022**, 29, 112308.
- [24] K. Zhang, W. Zholobenko, A. Stegmeir, K. Eder, F. Jenko, Magnetic flutter effect on validated edge turbulence simulations. Preprint. **2023** <https://arxiv.org/abs/2309.07763>
- [25] J. Peer, A. Kendl, T. Ribeiro, B. Scott, *Nucl. Fusion* **2017**, 57, 086026.
- [26] B. Zhu, X. Q. Xu, X. Z. Tang, *Nucl. Fusion* **2023**, 63, 086027. Not subject to copyright in the USA. Contribution of U.S. Department of Energy.

How to cite this article: R. Düll, H. Bufferand, E. Serre, G. Ciraolo, V. Quadri, N. Rivals, P. Tamain, *Contrib. Plasma Phys.* **2024**, e202300147. <https://doi.org/10.1002/ctpp.202300147>